OPEN ACCESS

Thermophysics & Energy ARTICLE

The Innovation Materials

Synergistic Yb/Mg dual-doping strategy for tabilizing the structure of high-voltage $LiCoO_2$

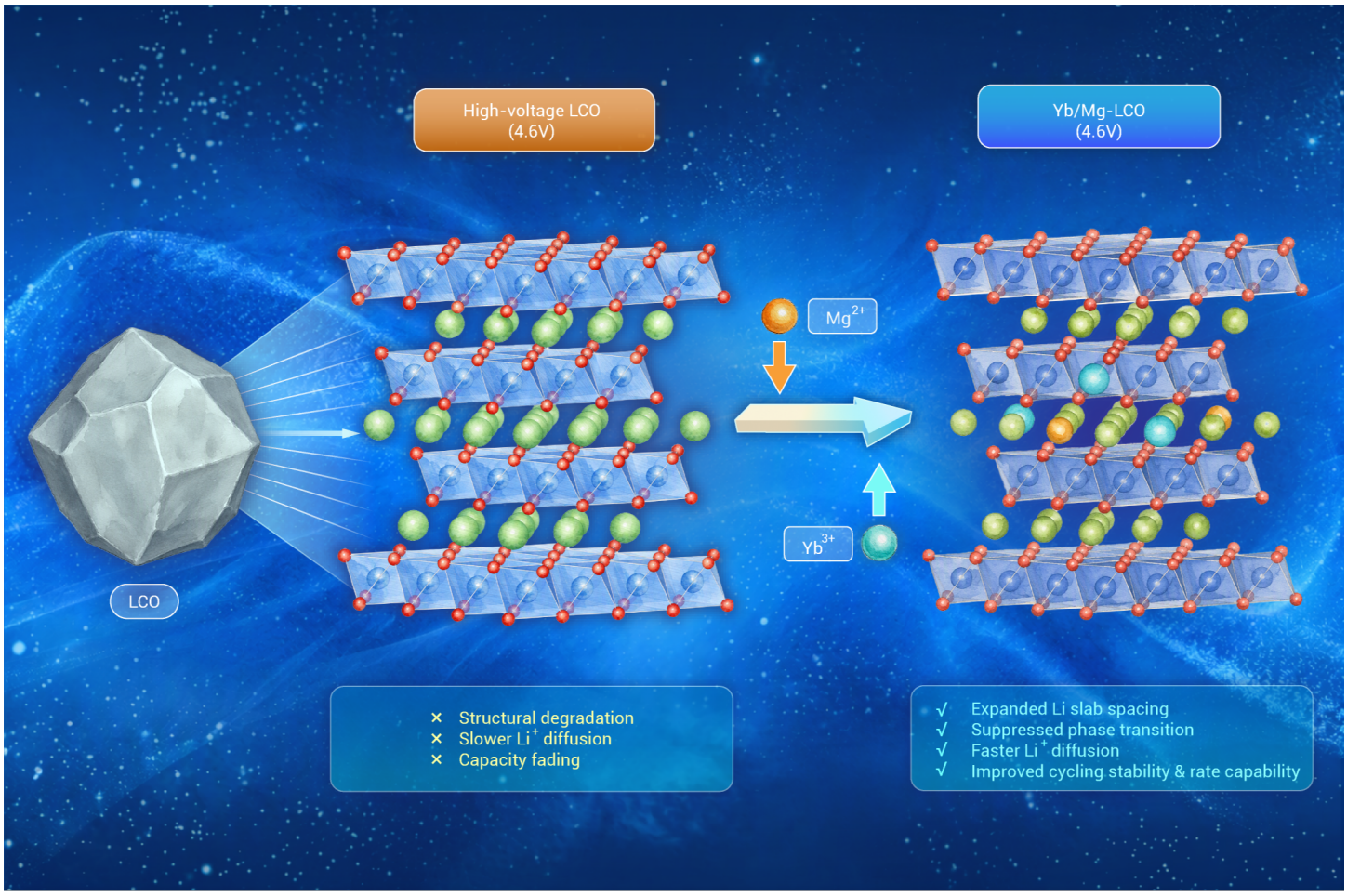
Jiaxing Wang,[1,3] Peng Shi,[1,3] Tao Zhou,[1] Teng Wang,[1] Zhangbin Cheng,[1] Jingfeng Wang,[2] and Guo Gao[1,*]

*Correspondence: guogao@sjtu.edu.cn

Received: January 22, 2026; Accepted: October 17, 2026; Published Online: October 20, 2026; https://doi.org/10.59717/j.xinn-mater.2026.100253

© 2026 The Author(s). This is an open access article under the CC BY license (https://creativecommons.org/licenses/by/4.0/).

GRAPHICAL ABSTRACT



PUBLIC SUMMARY

- High-voltage lithium cobalt oxide (LCO) suffers from structural degradation and rapid capacity fading.
- Ytterbium (Yb) and magnesium (Mg) co-doping improves the structural stability and lithium-ion transport of LCO.
- The co-doped LCO exhibits improved cycling stability and rate capability under high-voltage operation.

ARTICLE Thermophysics & Energy

OPEN ACCESS

Synergistic Yb/Mg dual-doping strategy for tabilizing the structure of high-voltage $LiCoO_2$

Jiaxing Wang,[1,3] Peng Shi,[1,3] Tao Zhou,[1] Teng Wang,[1] Zhangbin Cheng,[1] Jingfeng Wang,[2] and Guo Gao[1,*]

[1]School of Automation and Intelligent Sensing, Shanghai Jiao Tong University, Shanghai 200240, China

[2]National Engineering Research Center for Nanotechnology, 28 East Jiang Chuan Road, Shanghai, 200241, China

[3]These authors contributed equally

*Correspondence: guogao@sjtu.edu.cn

Received: January 22, 2026; Accepted: October 17, 2026; Published Online: October 20, 2026; https://doi.org/10.59717/j.xinn-mater.2026.100253

© 2026 The Author(s). This is an open access article under the CC BY license (https://creativecommons.org/licenses/by/4.0/).

Citation: Wang J., Shi P., Zhou T., et al. (2026). Synergistic Yb/Mg dual-doping strategy for tabilizing the structure of high-voltage $LiCoO_2$. *The Innovation Materials* **4**:100253.

Elevating the charging cutoff voltage of lithium cobalt oxide ($LiCoO_2$, LCO) beyond 4.5 V is the most direct approach to unlock its high theoretical capacity, yet it triggers detrimental phase transitions and rapid capacity degradation. To address this challenge, a synergistic doping strategy via ytterbium (Yb) and magnesium (Mg) is proposed to enhance the structural stability of LCO under high-voltage operation. A series of Yb doping and Yb/Mg doping LCO materials are synthesized via a conventional solid-state method. Comprehensive characterizations confirm that the larger-radius Yb^{3+} ions are successfully incorporated into the lattice, effectively expanding the Li slab spacing and enhancing thermal stability. Electrochemical evaluations reveal that an optimal Yb doping sample (10Y-LCO) delivers an improved capacity retention of 132 mAh g^{-1} after 250 cycles at 1 C, compared to 44.6 mAh g^{-1} for pristine LCO. Remarkably, the Yb/Mg doping sample (YM2-LCO) exhibits superior comprehensive performance, achieving a high reversible capacity, enhanced cycling stability, and excellent rate capability (126.1 mAh g^{-1} at 5 C). Mechanism studies through dQ/dV analysis and electrochemical impedance spectroscopy demonstrate that the doping effectively suppresses polarization growth and phase transition, while galvanostatic intermittent titration technique (GITT) results indicate a significantly enhanced lithium-ion diffusion coefficient. This work presents an effective doping protocol for developing high-voltage LCO cathodes with balanced stability and kinetics, offering valuable insights for the design of advanced layered oxide cathode materials.

INTRODUCTION

The growing demand for high-energy-density energy storage systems, driven by the rapid evolution of portable electronics and electric vehicles, has placed stringent requirements on lithium-ion battery technology.[1–5] Among various cathode materials, layered $LiCoO_2$ (LCO) remains the dominant choice in consumer electronics due to its high volumetric energy density, excellent rate capability, and mature manufacturing process.[6,7] However, the practical capacity of commercial LCO is limited to 140 mAh g^{-1} when cycled below 4.2 V, which is only about half of its theoretical value (274 mAh g^{-1}).[8,9] Pushing the charging cutoff voltage beyond 4.5 V is the most direct approach to unlock this latent capacity, but it triggers severe structural degradation and interfacial instability.[10,11] Specifically, deep delithiation induces irreversible phase transitions, leading to anisotropic lattice strain, microcrack generation, and eventual structural collapse.[12–15] Concurrently, the high-voltage environment generates highly oxidized Co^{4+} species and activates lattice oxygen.[16] These aggressive species accelerate electrolyte decomposition and promote cobalt dissolution, fostering a continuously thickening cathode-electrolyte interphase (CEI).[17] These intertwined degradation pathways collectively lead to the rapid capacity fade and raise serious safety concerns.[18]

Confronting these challenges, intensive research has focused on stabilizing the LCO lattice through elemental doping. Conventional strategies involving single-element substitution, such as Mg,[19,20] Al,[21] Ti,[22–24] Ni,[25,26] Mn,[27] or Zr,[28] have demonstrated partial success in suppressing specific degradation pathways. For instance, Mg doping is known to prevent the structural collapse along c direction at high voltage and to suppress the phase transition of O3-H3/M2,[29] while Al doping strengthens the metal-oxygen bonds.[11] More recently, rare-earth (RE) elements have emerged as particularly promising dopants due to their unique physicochemical properties.[30,31] Their large ionic radii can effectively pillar the Li slabs, mitigating c-axis contraction, while their strong oxygen affinity significantly stabilizes the lattice oxygen framework, thereby inhibiting oxygen release at high voltages.[32,33] Furthermore, co-doping strategies combining RE elements with other metal cations have also attracted increasing attention because they offer complementary regulation of structural stability and Li-ion transport.[33–35] However, despite these encouraging advances, most previous studies have primarily focused on electrochemical performance optimization, whereas the thermodynamic origin of dopant incorporation and the corresponding site preference remain insufficiently understood. In particular, the influence of realistic synthesis conditions on defect thermodynamics has rarely been considered, making it difficult to establish a clear relationship between dopant selection, incorporation behavior, and electrochemical performance. These unresolved issues highlight the need for a more rational co-doping strategy supported by both experimental validation and theoretical understanding.

To address these challenges, we herein design and implement a synergistic Yb/Mg dual-doping strategy to engineer high-voltage LCO cathodes. Yb^{3+} was selected because its relatively large ionic radius (compared with Co^{3+}) is expected to expand the interlayer spacing and stabilize the layered structure, while its relatively small size within the lanthanide series helps minimize excessive lattice distortion. Moreover, the strong Yb–O interaction is expected to enhance the stability of the oxygen framework during high-voltage cycling. Concurrently, Mg^{2+} is introduced to serve as a kinetic promoter, aimed at optimizing the charge compensation process and enhancing lithium-ion diffusion,[36,37] thus improving the rate performance that a sole Yb dopant may lack. Through a conventional solid-state synthesis route, we prepared a series of Yb doping, Mg doping and Yb/Mg doping LCO materials. A comprehensive suite of characterizations confirms the successful incorporation and uniform distribution of dopants. Electrochemical evaluations reveal that the optimal Yb/Mg doping cathode delivers a superior balance of properties. It not only retains the exceptional cycling stability endowed by Yb but also achieves a dramatically enhanced rate capability, significantly outperforming both the pristine and the best Yb doping counterparts.

Furthermore, DFT calculations under both conventional 0 K and experimentally relevant synthesis conditions were performed to reveal the influence of chemical potential on dopant incorporation. The combined experimental and theoretical analyses provide new insights into the thermodynamic origin of dopant site preference under practical synthesis conditions. These findings not only demonstrate the synergistic roles of Yb and Mg in regulating the structure and electrochemical behavior of high-voltage $LiCoO_2$, but also establish a defect-thermodynamic framework for understanding dopant incorporation under realistic synthesis conditions, providing useful guidance for the rational design of RE-assisted layered oxide cathodes.

MATERIALS AND METHODS

Material synthesis

All LCO samples were synthesized via the conventional high-temperature solid-state reaction. For the preparation of Yb doping samples, stoichiometric amounts of Li_2CO_3 (99.99%), Co_3O_4 (99.99%), and Yb_2O_3 (99.99%) were precisely weighed according to the nominal composition of Li : Co : Yb = 1.05 : 1 : x (x = 0, 0.005, 0.01, 0.02, 0.05). A 5% excess of lithium source was used to compensate for possible lithium volatilization during high-temperature calcination. The resulting samples were denoted as B-LCO (blank LCO), 05Y-LCO, 10Y-LCO, 20Y-LCO, and 50Y-LCO, corresponding to their Yb doping levels.

For the Yb/Mg doping samples, MgO (99.9%) was introduced as an additional precursor. Three different doping ratios were designed based on the optimal Yb content identified from the doping study: Yb : Mg = 0.005 : 0.005, 0.01 : 0.005, and 0.01 : 0.01 (relative to Co). These samples were labeled as YM1-LCO, YM2-LCO, and YM3-LCO, respectively.

For comparison, Mg single-doped LCO samples were also prepared under the same solid-state synthesis conditions. The Mg doping level was set to Li : Co : Mg = 1.05 : 1 : x (x = 0.005, 0.01, 0.015, 0.02), corresponding to 0.5%, 1.0%, 1.5%, and 2.0% Mg substitution relative to Co. The obtained samples were denoted as 05M-LCO, 10M-LCO, 15M-LCO, and 20M-LCO.

The synthesis procedure was identical for all samples. The raw powders were first mixed and ground in an agate mortar for 1 hour (dry mixing). Subsequently, an appropriate amount of anhydrous ethanol was added as a dispersing agent, followed by another 30 minutes of wet grinding to achieve a homogeneous mixture. The slurry was dried at 80°C in an oven, and the resulting agglomerates were ground again into fine, uniform precursor powder. Finally, the powder was placed in an alumina crucible and calcined in a muffle furnace. The calcination was conducted at 950°C for 10 hours with a heating rate of 5 °C min^{-1}, followed by natural cooling to room temperature. The sintered products were ground gently to obtain the final cathode materials.

Sample characterization

The crystal structure and phase purity of the synthesized powders were characterized by X-ray diffraction (XRD, Bruker D8 Advance) using Cu Kα radiation (λ = 1.5406 Å). Data were collected in the 2θ range of 10° to 80° with a step size of 0.02°. The morphology and particle size distribution of the samples were examined using a field-emission scanning electron microscope (FE-SEM, Hitachi SU 8100). Elemental distribution and homogeneity within the samples were analyzed via energy-dispersive X-ray spectroscopy (EDS) mapping, which was conducted in conjunction with the SEM observations. The surface chemical composition and valence states of the constituent elements were analyzed by X-ray photoelectron spectroscopy (XPS, Shimadzu AXIS Ultra DLD), with all binding energies calibrated against the C 1*s* peak at 284.8 eV.

Electrochemical measurement

The electrochemical performance was evaluated using CR2032 coin-type cells assembled in an argon-filled glovebox. The working electrode was prepared by mixing the active material, Super P conductive carbon, and polyvinylidene fluoride (PVDF) binder in a weight ratio of 8:1:1, using N-methyl-2-pyrrolidone (NMP) as the solvent to form a homogeneous slurry. The slurry was uniformly coated onto an aluminum foil current collector, dried at 80°C overnight in a vacuum oven, and then punched into discs with a diameter of 12 mm. High-purity lithium metal foil was used as the counter/reference electrode, and Celgard 2400 was employed as the separator. The electrolyte was 1.0 M $LiPF_6$ in a mixture of ethylene carbonate (EC), dimethyl carbonate (DMC), and ethyl methyl carbonate (EMC) (1:1:1 by volume). Galvanostatic charge-discharge tests, including long-term cycling and rate capability evaluations, were performed within a voltage window of 3.0–4.6 V (vs. Li^+/Li) at 25°C using a LANHE CT3002A battery test system. Prior to high-rate testing, the cells were activated by cycling three times at 0.1 C. Galvanostatic intermittent titration technique (GITT) measurements were also conducted on the same system to determine the lithium-ion diffusion coefficients. A small current pulse (0.1 mA) was applied for 10 min followed by an open-circuit relaxation for 30 min, and this process was repeated throughout the charge/discharge profile. The differential capacity (dQ/dV) analysis was derived from the galvanostatic charge-discharge profiles to precisely identify phase transition potentials and evaluate polarization evolution. Cyclic voltammetry (CV) and electrochemical impedance spectroscopy (EIS) tests were carried out on a CHI660E electrochemical workstation. CV scans were performed at a scan rate of 0.1 mV s^{-1} between 3.0 and 4.6 V, while EIS measurements were conducted over a frequency range from 100 kHz to 0.01 Hz with an amplitude of 5 mV.

Density functional theory (DFT) calculations

First-principles calculations were performed using the Vienna Ab initio Simulation Package (VASP) based on DFT.[38,39] The projector augmented-wave (PAW) method was employed to describe the ion-electron interactions,[40,41] while the exchange-correlation energy was treated within the generalized gradient approximation (GGA) using the Perdew-Burke-Ernzerhof (PBE) functional.[42] A plane-wave cutoff energy of 500 eV was adopted, and the Brillouin zone was sampled using a Γ-centered 3 × 3 × 1 k-point mesh. The electronic self-consistency criterion was set to 10^{-5} eV, and all atomic positions and lattice parameters were fully relaxed until the residual force on each atom was below 0.02 eV/Å.

To evaluate the preferential occupation sites of Yb and Mg dopants in $LiCoO_2$, the substitutional defect formation energy (E_{form}) for Li-site and Co-site doping was calculated according to:

$$E_{form} = E_{doped} - E_{pristine} - \sum_i n_i \mu_i$$

where E_{doped} and $E_{pristine}$ are the total energies of the doped and pristine $LiCoO_2$ supercells, respectively. n_i denotes the number of atoms of species i added ($n_i > 0$) or removed ($n_i < 0$), and μ_i is the corresponding chemical potential.

The chemical potentials of Li, Co, Mg, and Yb were determined from the thermodynamic equilibrium conditions of Li_2O, Co_3O_4, MgO, and Yb_2O_3, respectively. The elemental chemical potentials were referenced to the corresponding binary oxides, which are thermodynamically consistent with the oxide precursors and oxygen-containing atmosphere employed during the high-temperature solid-state synthesis. Such a treatment provides a more realistic description of the chemical environment during sample preparation than using elemental metals as reference reservoirs. Specifically, the elemental chemical potentials satisfy the following thermodynamic equilibrium relationships:

$$2\mu_{Li} + \mu_O = \mu_{Li_2O}$$

$$3\mu_{Co} + 4\mu_O = \mu_{Co_3O_4}$$

$$\mu_{Mg} + \mu_O = \mu_{MgO}$$

$$2\mu_{Yb} + 3\mu_O = \mu_{Yb_2O_3}$$

The oxygen chemical potential was corrected considering the experimental synthesis condition (950°C, air atmosphere) using JANAF thermodynamic data:[43,44]

$$\mu_O(T,p) = \frac{1}{2}E_{tot}(O_2) + \Delta\mu_O(T,p^0) + \frac{1}{2}k_B T \ln\left(\frac{p_{O_2}}{p^0}\right)$$

where $E_{tot}(O_2)$ is the DFT total energy of an oxygen molecule, k_B is the Boltzmann constant, T is the absolute temperature, p_{O_2} is the oxygen partial pressure in the reaction atmosphere, and p^0 is the standard pressure. The temperature-dependent correction $\Delta\mu_O(T,p^0)$ was obtained from the JANAF thermochemical tables using the tabulated enthalpy and entropy data of gaseous O_2. The resulting oxygen chemical potential was subsequently used to determine the elemental chemical potentials under the experimental synthesis environment. This treatment enables the defect formation energies to be evaluated under thermodynamic conditions that closely resemble the experimental solid-state synthesis process, providing a more realistic description of dopant site preference than calculations performed under the idealized 0 K limit.

RESULTS AND DISCUSSION

Structural and elemental characterization

The crystal structure and phase purity of all synthesized samples were first examined by XRD. As shown in Figure 1, all diffraction peaks for the Yb (B-LCO, 05Y-LCO, 10Y-LCO, 20Y-LCO, 50Y-LCO), the Mg doping series (05Mg-LCO, 10Mg-LCO, 15Mg-LCO, and 20Mg-LCO), and Yb/Mg doping series (YM1-LCO, YM2-LCO, YM3-LCO) can be precisely indexed to the layered α-$NaFeO_2$ structure (space group R-3m) of $LiCoO_2$ (PDF#50-0653), with no detectable impurity phases. These results indicate that the introduced dopants are well accommodated within the layered $LiCoO_2$ structure without disrupting the

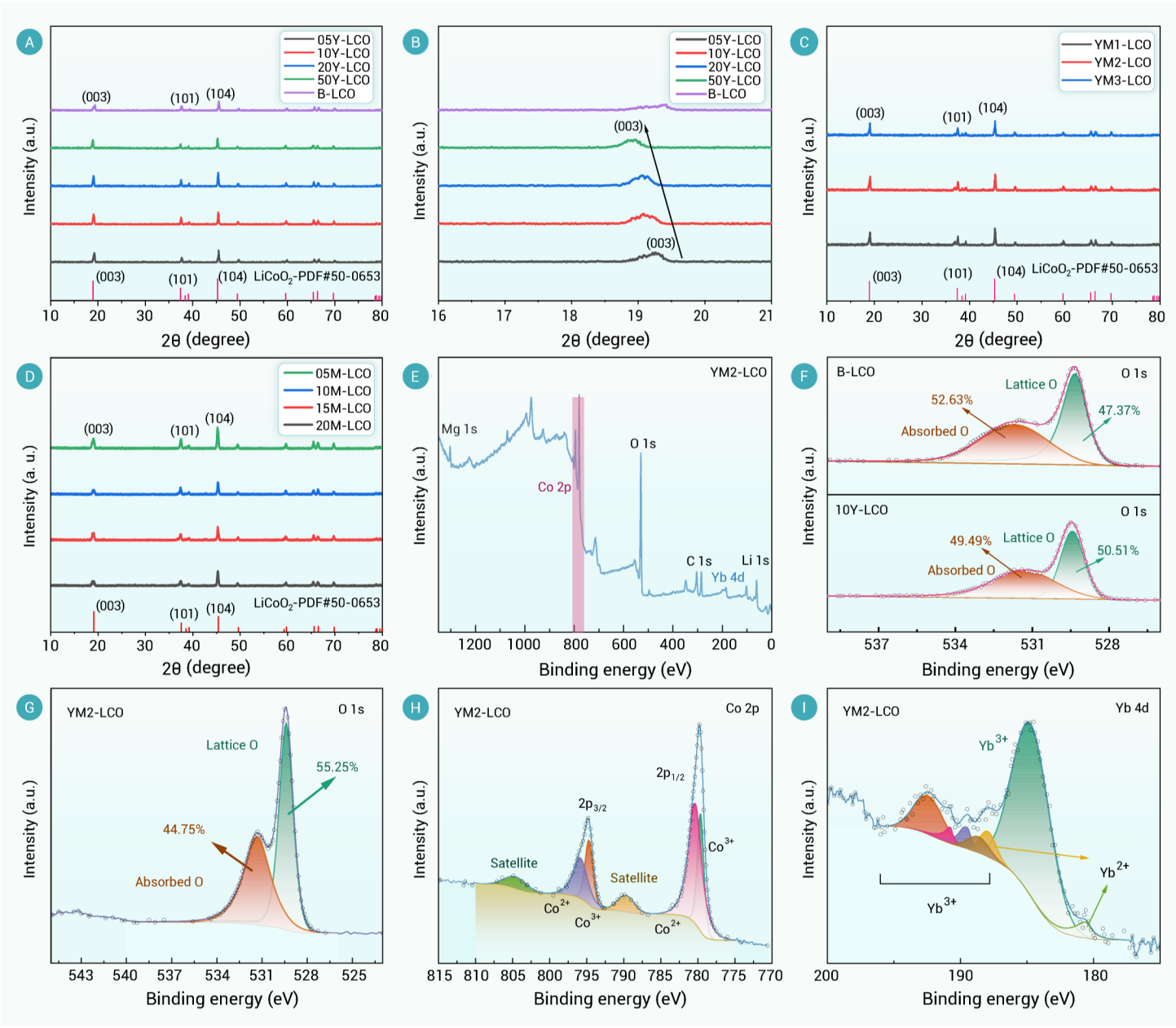


Figure 1. Structural and chemical state analysis of the synthesized LCO samples XRD patterns: (A) full patterns of LCO with different Yb contents, (B) enlarged (003) peak region of (A), (C) full patterns of Yb/Mg doping LCO, and (D) full patterns of Mg-doped LCO with different Mg contents. XPS analysis of representative samples: (E) survey spectrum of YM2-LCO, and high-resolution spectra of (F) O 1s for B-LCO and 10Y-LCO, (G) O 1s, (H) Co 2p, and (I) Yb 4d for YM2-LCO.

fundamental crystal framework. A closer inspection of the (003) diffraction peak, which is highly sensitive to the interlayer spacing, reveals insightful changes (Figure 1B). With increasing Yb doping content, the (003) peak systematically shifts toward lower angles. According to Bragg's law, this shift indicates a distinct expansion of the interlayer spacing along the c-axis, which is directly attributed to the substitution of larger Yb^{3+} ions (0.86 Å) for the smaller Co^{3+} ions (0.61 Å) in the transition metal layers, effectively acting as a structural pillar.

The surface chemical composition and electronic states of the constituent elements were analyzed in detail by XPS. The survey spectrum of the optimal Yb/Mg doping sample (YM2-LCO) confirms the presence of Co, O, Yb, and Mg, along with adventitious carbon, with no other impurities detected (Figure 1E). High-resolution spectra provide deeper insights into the chemical environment. The O 1*s* spectrum (Figure 1G) can be deconvoluted into two primary contributions: the lattice oxygen (O_{lat}) at a binding energy of 529.2 eV, and surface adsorbed oxygen species (O_{ads}, e.g., hydroxyls, carbonates) at 531.3 eV. Quantitative analysis shows that the relative area percentage of the O_{lat} component increases from 47.37% in pristine B-LCO (Figure 1F) to 50.51% in Yb-doped 10Y-LCO, and further to 55.25% in YM2-LCO. It indicates that after the Yb-Mg doping modification, a stronger metal-O bond is formed.[45] This progressive increase in the lattice oxygen fraction signifies a strengthened and more stable metal oxygen bonding upon Yb and Mg doping, which is crucial for suppressing oxygen evolution at high voltages.[46]

Further analysis of the high-resolution XPS spectra corroborates the successful doping and its impact. The Co 2*p* spectrum of YM2-LCO (Figure 1H) exhibits the characteristic spin-orbit doublets (Co $2p_{3/2}$ and Co $2p_{1/2}$) along with their satellite peaks, with binding energies consistent with the predominant Co^{3+} oxidation state. This indicates that the introduction of Yb and Mg did not induce a significant change in the average cobalt valence. The presence and chemical state of Yb are unequivocally confirmed by the Yb 4*d* spectrum (Figure 1I). The spectrum can be fitted with two pairs of spin-orbit split peaks, corresponding to Yb^{3+} (the dominant state) and a minor amount of Yb^{2+}. This verifies that Yb has been effectively incorporated into the material, predominantly in the trivalent state as intended from the Yb_2O_3 precursor.

The morphology and elemental distribution of the materials were investigated by SEM and EDS. As shown in Figures 2A-C, all samples exhibit typical

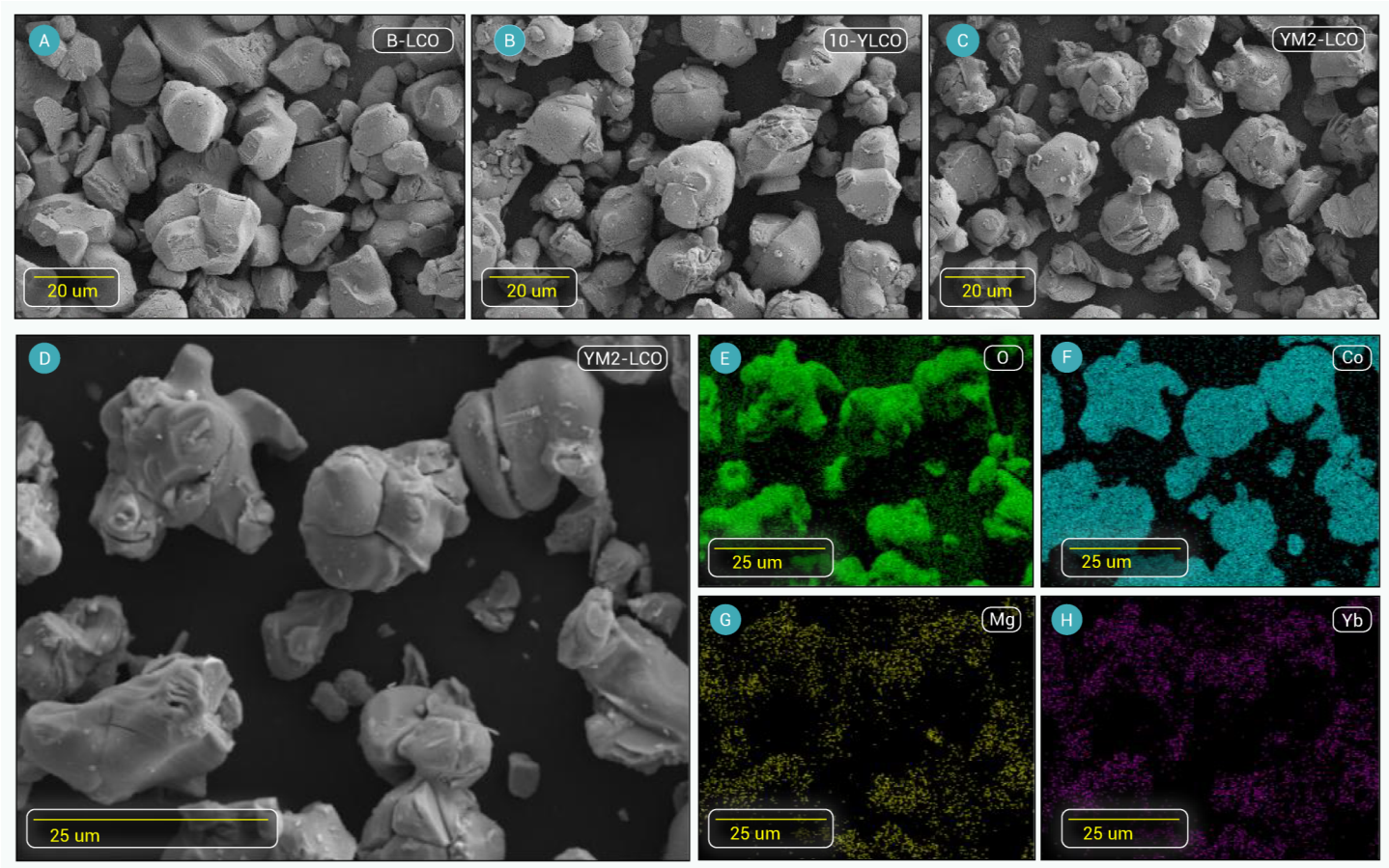


Figure 2. Morphological and elemental distribution analysis SEM images of (A) B-LCO, (B) 10Y-LCO, and (C) YM2-LCO. (D) SEM image of the scanning area for YM2-LCO and the corresponding EDS elemental mapping for (E) O, (F) Co, (G) Mg, and (H) Yb.

polyhedral particle morphologies characteristic of high-temperature solid-state synthesized LCO. The pristine B-LCO particles (Figure 2A) display smooth surfaces and clear edges. With Yb doping (10Y-LCO, Figure 2B) and further Yb/Mg doping (YM2-LCO, Figure 2C), the primary particle size shows a slight reduction and the surfaces become somewhat rougher, which could be attributed to the doping elements altering the diffusion behavior and grain growth kinetics during the high-temperature calcination process. In particular, the lattice distortion induced by doping and the relatively large ionic radius of Yb^{3+} may inhibit particle fusion during the solid-state synthesis process, resulting in smaller primary particles and relatively rougher surfaces. Meanwhile, the non-uniform crystal growth and altered surface diffusion behavior may contribute to relatively rougher particle surfaces. Notably, the particles remain clearly separated without severe agglomeration.

To verify the uniformity of dopant distribution within the YM2-LCO sample, EDS elemental mapping was performed on a selected particle agglomerate (Figure 2D). The corresponding maps for O, Co, Mg, and Yb are presented in Figures 2E-H. The signals for O and Co are uniformly bright and cover the entire scanned area, confirming the homogeneity of the LCO matrix. Crucially, the signals for the dopants, Mg and Yb, also exhibit a highly homogeneous spatial distribution that perfectly overlaps with the Co and O maps, with no signs of segregation or clustering. This result provides direct visual evidence that both Mg and Yb are successfully and uniformly incorporated into the LCO host particles at the microscale, forming a uniform doped phase essential for consistent electrochemical performance.

Electrochemical performance

The electrochemical performance of all samples was systematically evaluated in lithium half-cells within a voltage window of 3.0–4.6 V (vs. Li^+/Li). Figure 3 presents a comparative analysis of cycling stability, rate capability, and representative voltage profiles. The long-term cycling stability at a 1C (220 mA g^{-1}) is depicted in Figures 3A-C. For the Yb doping series (Figure 3A), the pristine B-LCO suffers from rapid capacity decay, retaining only 44.6 mAh g^{-1} after 250 cycles. Doping with Yb significantly mitigates this fading. The optimal doping sample, 10Y-LCO (1% Yb), delivers a substantially improved capacity of 132 mAh g^{-1} after the same number of cycles, along with a nearly 100% average Coulombic efficiency, highlighting the effectiveness of Yb in stabilizing the structure during repeated Li^+ extraction/insertion.

For the Mg single-doping series (Figure 3C), Mg incorporation also improves the cycling stability compared with pristine B-LCO. Among the investigated samples, 05Mg-LCO exhibits the best electrochemical performance, delivering a discharge capacity of 78 mAh g^{-1} after 250 cycles. However, further increasing the Mg content leads to a gradual decline in cycling performance, suggesting that excessive Mg doping may adversely affect the electrochemical activity of $LiCoO_2$.

Introducing Mg alongside Yb further modulates the cycling performance, as shown in Figure 3B. Among the doping samples, YM2-LCO (1% Yb, 0.5% Mg) exhibits the best balance, delivering a capacity retention comparable to that of 10Y-LCO after 250 cycles while maintaining excellent Coulombic efficiency throughout the test. Samples with excessively high dopant concentrations (50Y-LCO and YM3-LCO) show inferior cycling, indicating the importance of an optimal doping level. Notably, after 250 cycles, YM2-LCO delivers a higher discharge capacity than both 05Mg-LCO and 15Mg-LCO. Compared with 05Mg-LCO, which contains the same Mg content (0.5%) as YM2-LCO, the discharge capacity of YM2-LCO is increased by 69%. These results indicate that the improved electrochemical performance cannot be simply attributed to the dopant amount, but rather arises from the synergistic interaction between Yb and Mg.

The rate capabilities of the samples are compared in Figures 3D-E. At low current densities (≤ 0.5 C), all doped samples deliver higher reversible capacities than B-LCO. As the rate increases, their performance diverges markedly (Figure 3D). While 10Y-LCO shows a clear improvement over B-LCO, its capacity at 5 C is still limited. Remarkably, the Yb/Mg doping samples, partic-

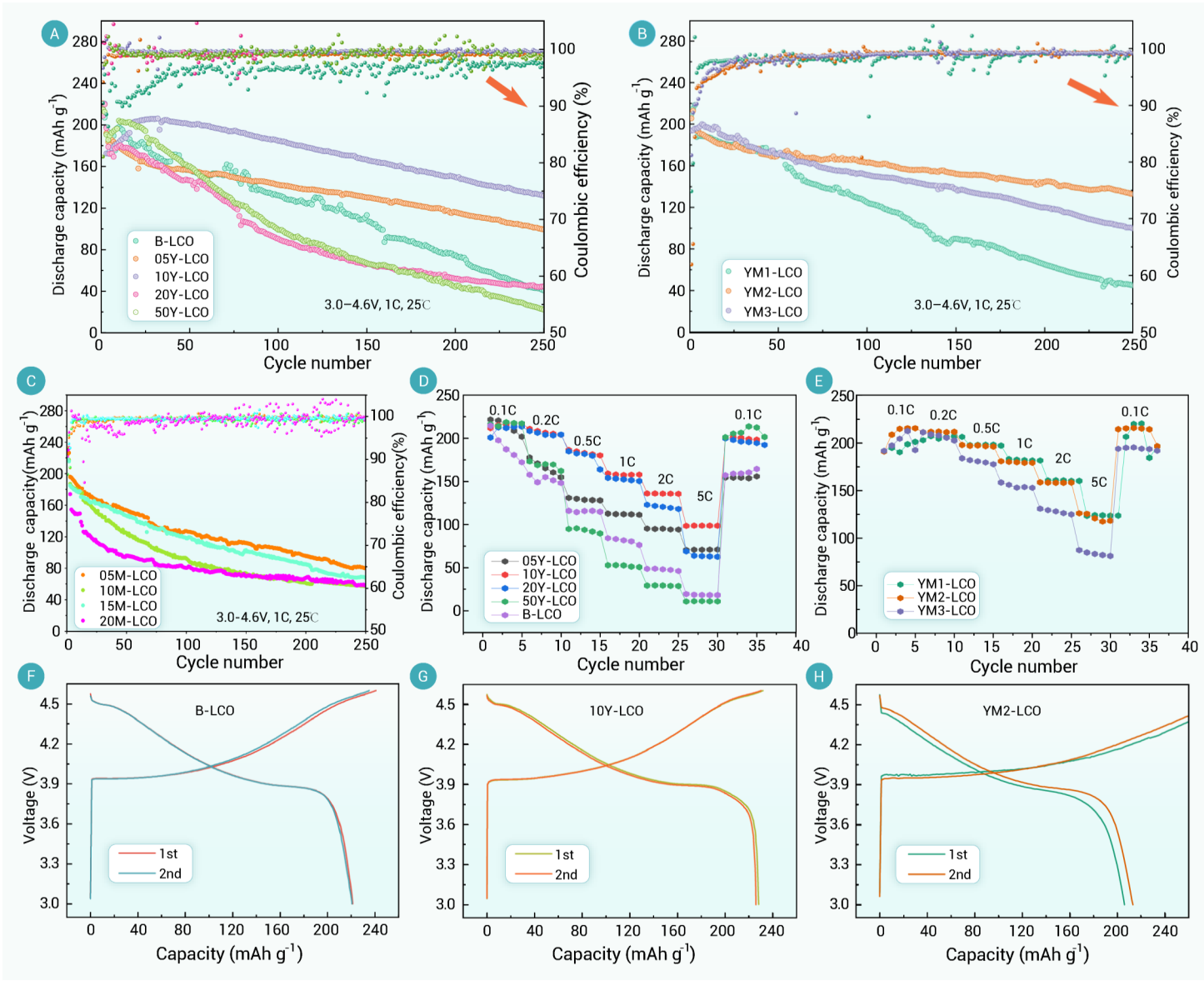


Figure 3. Electrochemical performance comparison in a voltage window of 3.0–4.6 V (vs. Li^+/Li) Cycling performance at 1 C of (A) Yb-doped, (B) Yb/Mg co-doped, and (C) Mg-doped LCO samples. Rate capability of (D) Yb-doped and (E) Yb/Mg co-doped LCO samples. Galvanostatic charge/discharge profiles of (F) B-LCO, (G) 10Y-LCO, and (H) YM2-LCO at 0.1 C for the initial two cycles.

ularly YM2-LCO, demonstrate superior rate performance (Figure 3E). YM2-LCO retains a high discharge capacity of 126.1 mAh g^{-1} even at a demanding 5 C rate, significantly outperforming all other samples including 10Y-LCO. The capacity retention at 5 C relative to 0.1 C reaches approximately 59%. When the rate is returned to 0.1 C, the capacity of YM2-LCO fully recovers, confirming the excellent structural reversibility and kinetic advantages imparted by the doping.

The galvanostatic charge and discharge profiles at 0.1 C for the initial two cycles are shown in Figures 3F-H. While all samples exhibit the characteristic voltage plateaus of LCO, the evolution from the 1st to the 2nd cycle reveals distinct activation behaviors. For the pristine B-LCO (Figure 3F) and the Yb-doped 10Y-LCO (Figure 3G), the nearly perfect overlap of their discharge curves indicates minimal change in polarization within the first two cycles. This suggests that for these materials, the primary degradation mechanisms, such as severe structural collapse in B-LCO and the gradual strain accumulation countered by Yb doping in 10Y-LCO, dominate long-term failure but are not prominently reflected in the initial activation kinetics under mild conditions. In clear contrast, the YM2-LCO (Figure 3H) displays a discernibly higher discharge plateau in the 2nd cycle. This signifies a reduction in polarization after the initial activation, which is a direct indicator of more favorable interfacial kinetics and a rapidly stabilized electrode and electrolyte interface.

To gain deeper insight into the redox reversibility and structural evolution during cycling, CV and dQ/dV analysis were performed. The CV curves at 0.1 mV s^{-1} are shown in Figures 4A–C. The peak potential separation ($\Delta E_p = E_{pa} - E_{pc}$) was quantitatively extracted from the anodic and cathodic peak potentials of each CV profile to compare the polarization and electrochemical reversibility among different samples. For pristine B-LCO (Figure 4A), the peak currents notably decrease with cycling, while the anodic peak shifts to higher potentials and the cathodic peak shifts to lower potentials, leading to a continuous increase in ΔE_p from approximately 0.21 V in the 1st cycle to 0.28 V in the 10th cycle and 0.36 V in the 50th cycle. This behavior reflects severe electrode polarization and structural deterioration. In contrast, the Yb-doped 10Y-LCO (Figure 4B) exhibits increased peak currents in early cycles, with the anodic and cathodic peaks shifting towards each other and a consequent decrease in ΔE_p from approximately 0.34 V in the 1st cycle to 0.22 V in the 10th cycle and 0.14 V in the 50th cycle. These features correspond to a lower overpotential and enhanced electrochemical reversibility introduced by Yb doping. Among the doping samples, YM2-LCO (Figure 4C) presents the most stable CV profiles, with minimal peak current decay and the smallest variation in peak positions over 50 cycles. The ΔE_p values of YM2-LCO remain relatively low and stable, changing only from approximately 0.29 V in the 1st cycle to 0.13 V in the 10th cycle and 0.10 V in the 50th cycle, confirm-

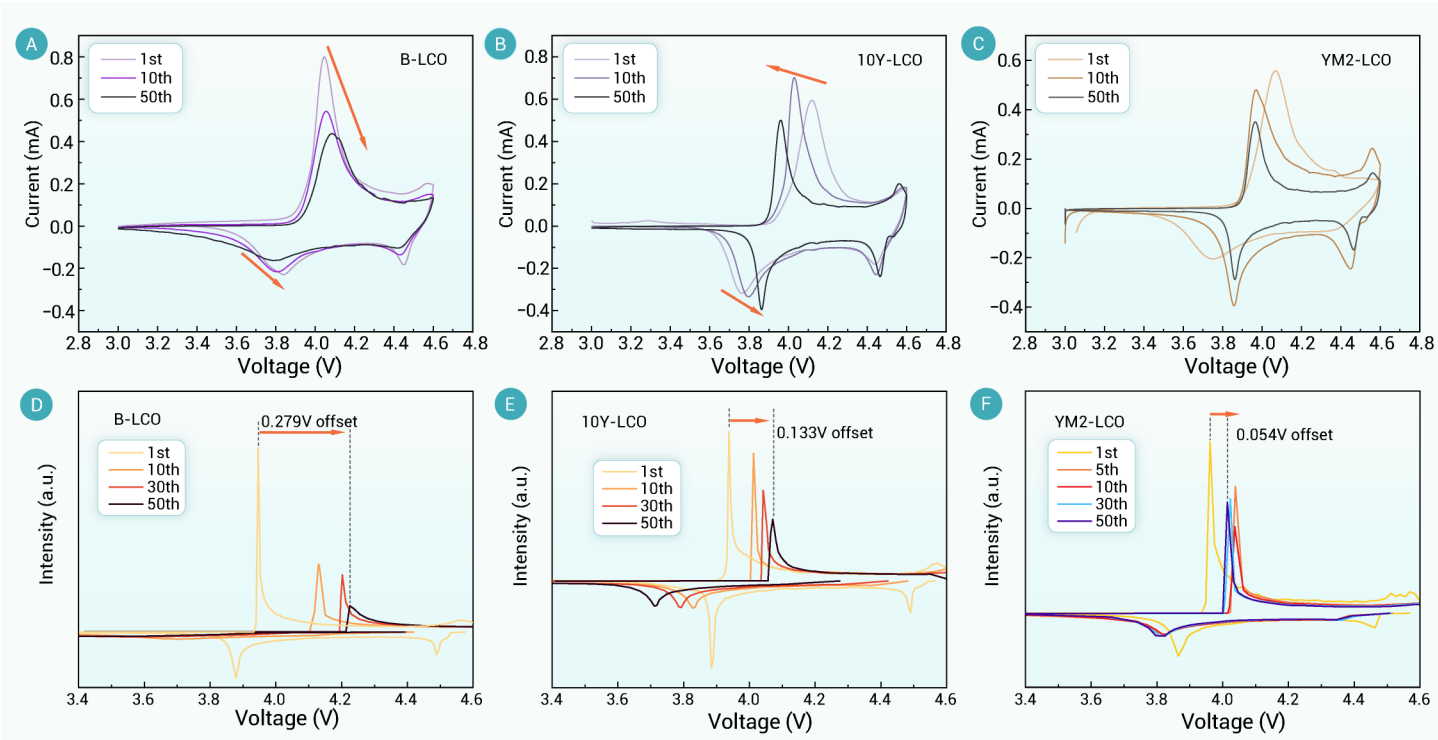


Figure 4. Cyclic voltammetry and differential capacity analysis CV curves at 0.1 mV s^{-1} for (A) B-LCO, (B) 10Y-LCO, and (C) YM2-LCO. Corresponding dQ/dV curves derived from the 1st, 10th, 30th, and 50th galvanostatic cycles for (D) B-LCO, (E) 10Y-LCO, and (F) YM2-LCO.

ing the suppressed polarization and superior redox reversibility enabled by Yb/Mg co-doping.

The phase transition behavior and detailed polarization evolution were further quantified by dQ/dV analysis (Figures 4D–F). In B-LCO (Figure 4D), the characteristic oxidation peak shifts continuously to higher voltages by 0.279 V from the 1st to the 50th cycle, while the reduction peak severely attenuates and broadens, revealing pronounced structural instability and irreversible phase transitions. This weakened and broadened reduction response indicates the deteriorated reversibility of the high-voltage structural evolution during deep delithiation of LCO, including the sequential structural evolution from the O3 phase through the H1/M/H2/H3 phases and the subsequent evolution toward a highly delithiated O1-type stacking configuration accompanied by slab gliding. Such irreversible structural evolution disrupts the CoO_2-layer stacking, increases electrochemical polarization, and progressively impairs the reversibility of Li^+ extraction/insertion. The 10Y-LCO sample (Figure 4E) shows a marked improvement, with the oxidation peak shifting only 0.133 V and the reduction peak maintaining its sharp shape and intensity, consistent with the stabilizing effect of Yb doping. This retention of the redox features suggests that Yb doping partially suppresses the irreversible structural evolution associated with these high-voltage phase transitions and improves their reversibility. The dQ/dV profiles of the optimal doping sample, YM2-LCO (Figure 4F), display exceptional stability. Although its oxidation peak shows a total shift of 0.054 V over 50 cycles, the key observation is its steady shift toward lower voltages throughout the entire test. This consistent leftward shift, in contrast to the reversible shifts observed in YM1-LCO and YM3-LCO, suggests a progressive reduction in the polarization associated with the oxidation reaction. Moreover, the highly overlapped and sharp redox peaks indicate that Yb/Mg co-doping more effectively preserves the reversibility of the high-voltage structural evolution and mitigates irreversible degradation, particularly the structural distortion and slab gliding associated with the evolution toward highly delithiated O1-type configurations. Therefore, the Yb/Mg doping in YM2-LCO enables continuous optimization of the reaction kinetics during long-term cycling, thereby underpinning its superior capacity retention.

Kinetics analysis and electrochemical mechanisms

To gain deeper insight into the electrochemical behavior and the mechanistic role of the dopants, detailed kinetic analyses focusing on charge transfer and solid-state ion diffusion were performed. The evolution of interfacial charge transfer kinetics was investigated through EIS. The Nyquist plots, fitted with appropriate equivalent circuits, are presented in Figure 5. Before the formation cycle (Figures 5A & C), all doped samples exhibited a lower charge-transfer resistance (R_{ct}) compared to the pristine B-LCO, indicating a more favorable initial interface for lithium-ion migration. Notably, the optimal Yb/Mg doping sample (YM2-LCO) showed the smallest semicircle diameter. After 50 cycles at 1 C (Figures 5B & D), the R_{ct} for all samples increased due to interfacial evolution and possible CEI growth. However, the degradation was most severe for B-LCO. The doped samples, especially the doping YM2-LCO, demonstrated superior interfacial stability, maintaining the lowest R_{ct} after prolonged cycling. This enhanced stability is likely correlated with the greater structural tolerance of the doped materials against detrimental high-voltage phase transitions.[33]

To probe the lithium-ion transport kinetics within the bulk material, the GITT was employed. Representative GITT curves for B-LCO and 10Y-LCO are shown in Figures 6A-B, respectively. The voltage polarization (ΔE_t) observed during the current pulses was consistently smaller for the doped 10Y-LCO than for B-LCO, suggesting reduced internal resistance. The lithium-ion chemical diffusion coefficients (D_{Li^+}) were calculated from the GITT relaxation profiles. As shown in Figures 6C-D (2nd cycle), the D_{Li^+} values for the doped samples were significantly higher than those of B-LCO across most of the charge/discharge window. The Yb/Mg doping samples exhibited the highest D_{Li^+} values, often exceeding those of B-LCO by nearly an order of magnitude. This advantageous kinetic characteristic was well-preserved after 50 cycles (Figures 6E-F). While the D_{Li^+} for B-LCO became irregular, likely due to accumulated structural damage, the doped samples, particularly the doping ones, maintained high and stable ion mobility. The superior and sustained lithium-ion diffusivity in YM2-LCO provides a direct kinetic explanation for its exceptional rate capability.

Integrating the findings from EIS and GITT, a coherent picture of the Yb/Mg synergistic mechanism emerges. The EIS results highlight the role of doping in maintaining a stable, low-resistance interface, a benefit crucial for long-term cycling. The GITT derived D_{Li^+} values unequivocally demonstrate that doping, especially with Mg, drastically enhances the bulk solid-state lithium-ion diffusion. This suggests that Yb doping primarily reinforces the structural

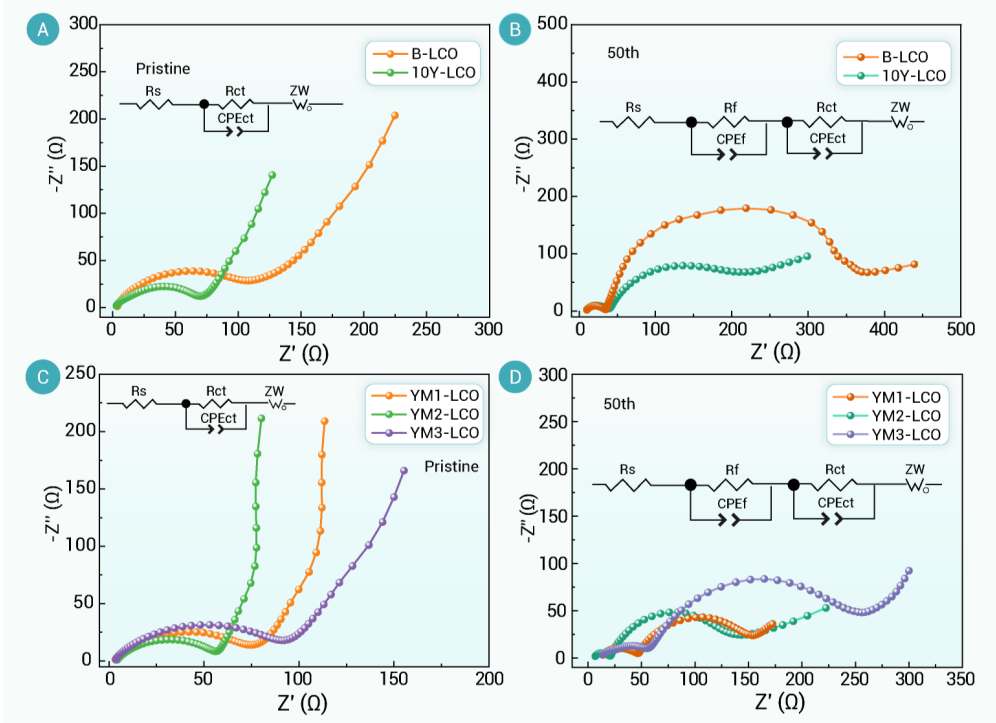


Figure 5. Electrochemical impedance analysis Nyquist plots of B-LCO and 10Y-LCO (A) before formation and (B) after 50 cycles, and of Yb/Mg co-doped LCO samples (C) before formation and (D) after 50 cycles.

framework, providing lasting stability, while Mg doping is key to optimizing the charge compensation process and ion transport pathways. Therefore, the Yb/Mg doping strategy successfully decouples two critical aspects: Yb ensures structural durability to sustain the lattice over cycles, while Mg provides fast ionic transport to enable high rate performance. This complementary action is the fundamental reason why the doping cathode achieves a superior balance of properties, overcoming the typical trade-off between cycling stability and rate capability in high-voltage LCO.

DFT investigation of dopant site preference

To clarify the preferential occupation sites of Yb and Mg in layered $LiCoO_2$, DFT calculations were performed by evaluating the substitutional formation energies at both Li and Co sites. In addition to the conventional zero-temperature approximation, the oxygen chemical potential was corrected according to the experimental synthesis condition (950°C in air) using JANAF thermodynamic data, enabling the defect thermodynamics to better represent the realistic solid-state reaction environment. The calculated formation energies under both conventional 0 K conditions and experimentally relevant synthesis conditions are summarized in Figure 7.

At the conventional 0 K limit, both Yb and Mg exhibit significantly lower formation energies at the Co site than at the Li site (Figure 7A), indicating that transition-metal-site substitution is thermodynamically preferred. This tendency originates from the chemical potential equilibrium established using the corresponding binary oxides.

As shown in Figure 7B, after introducing the temperature- and oxygen-pressure-dependent correction to the oxygen chemical potential, the defect

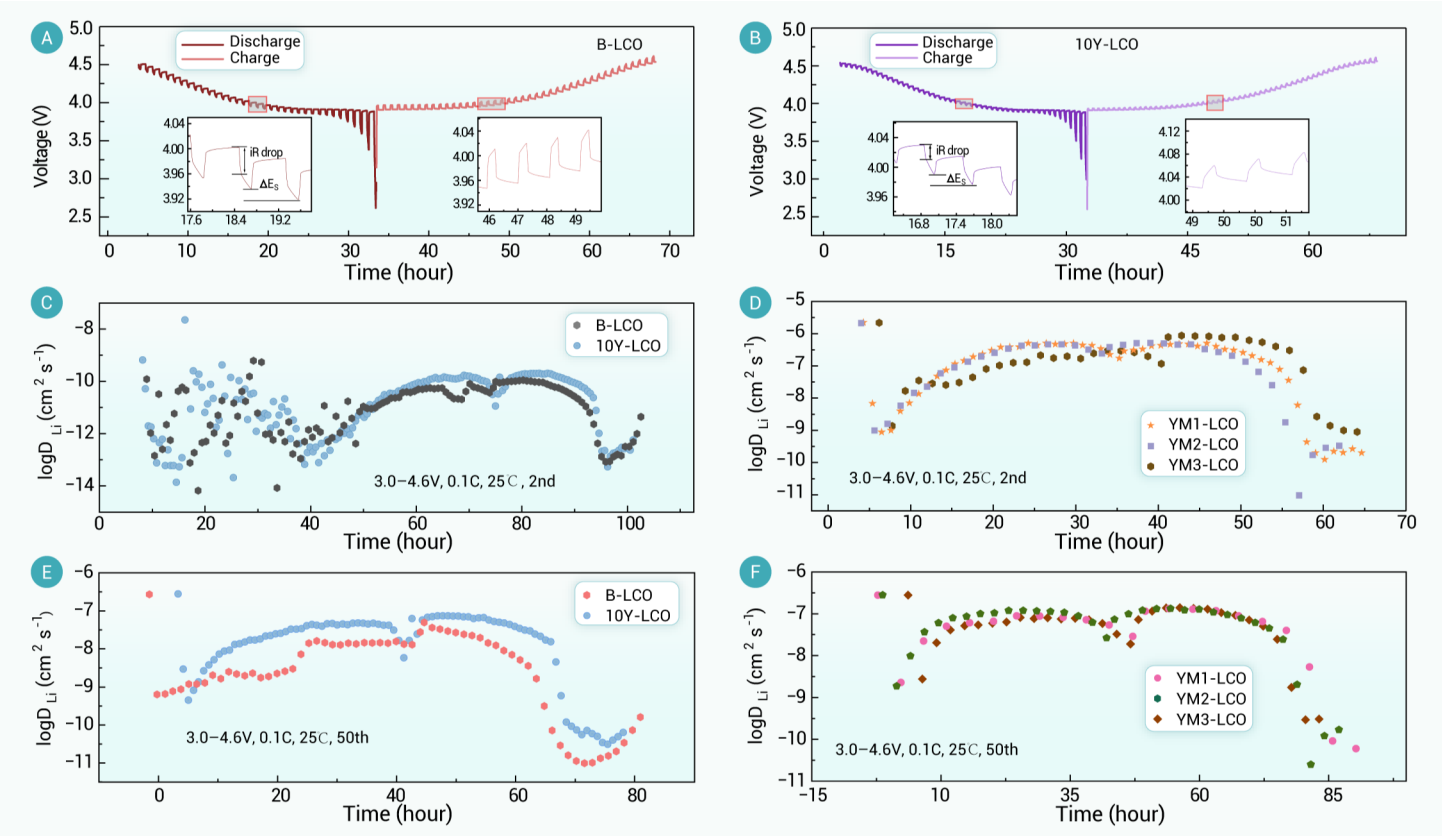


Figure 6. Electrochemical kinetics analysis based on GITT GITT profiles of (A) B-LCO and (B) 10Y-LCO. Lithium-ion diffusion coefficients calculated from the GITT data for (C) B-LCO and 10Y-LCO and (D) YM2-LCO at the 2nd cycle, and for (E) B-LCO and 10Y-LCO and (F) YM2-LCO at the 50th cycle.

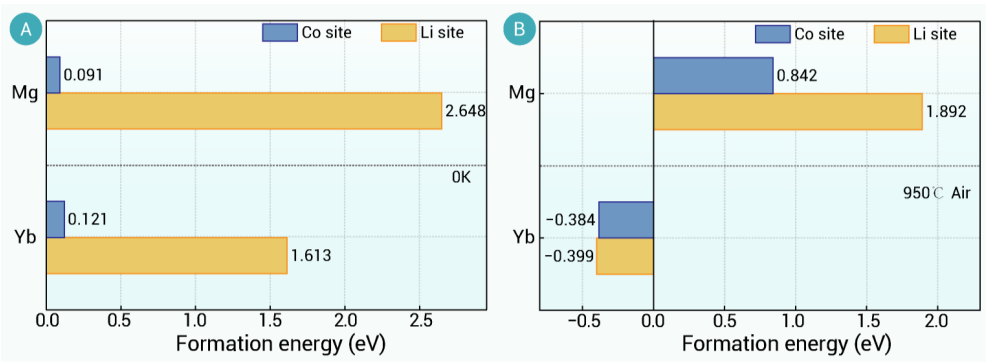


Figure 7. Calculated formation energies of Yb and Mg substitution defects at Li and Co sites in $LiCoO_2$ under different chemical potential conditions (A) Uncorrected DFT formation energies at 0 K. (B) Formation energies corrected by oxygen chemical potential under experimental synthesis conditions (950°C, air).

formation energies change substantially. For Yb, both Li-site and Co-site substitutions become thermodynamically favorable, and the formation energy difference between the two configurations decreases to only 0.015 eV. Such a small energy difference suggests that Yb exhibits no strong site selectivity under the experimental synthesis conditions, and occupation of either crystallographic site is energetically possible. Similarly, the formation energies of Mg decrease after considering the realistic synthesis atmosphere. Although substitution at the Co site remains thermodynamically more favorable than that at the Li site, the energy difference between the two configurations is considerably reduced compared with the 0 K approximation, indicating that the predicted site preference is sensitive to the chemical potential conditions adopted in the calculations.

It should be noted that the calculated formation energies mainly describe the intrinsic thermodynamic preference of isolated substitutional defects, whereas the experimentally realized dopant distribution may also be influenced by additional factors during high-temperature synthesis. For Mg doping, the valence difference between Mg^{2+} and Co^{3+} may induce local charge compensation or defect formation, which could modify the relative stability of different Mg configurations under specific chemical environments. Meanwhile, the comparable ionic radii of Mg^{2+} and Li^{+} may facilitate Mg incorporation into Li layers during solid-state diffusion, while migration between different crystallographic layers may require additional structural rearrangement. Therefore, the final Mg distribution in $LiCoO_2$ may not be determined solely by the calculated isolated defect formation energies but could involve the combined effects of thermodynamic stability, defect chemistry, and kinetic processes.

For Yb doping, the nearly identical formation energies of Li-site and Co-site substitution under realistic synthesis conditions indicate that Yb incorporation is not strongly site-selective. Although Yb^{3+} substitution at the Co site is favorable due to the isovalent relationship with Co^{3+}, the small energy difference suggests that Li-site occupation cannot be excluded under experimental synthesis conditions. Therefore, the final Yb distribution may also be affected by synthesis parameters and kinetic factors.

Overall, the present calculations indicate that the intrinsic dopant site preference strongly depends on the chemical potential environment, while the final cation distribution in synthesized $LiCoO_2$ is likely governed by the combined effects of thermodynamic stability, defect compensation, and kinetic processes. Compared with the conventional zero-temperature approximation, incorporation of the experimentally relevant temperature and oxygen partial pressure produces a more realistic thermodynamic description of dopant incorporation during high-temperature solid-state synthesis. Considering the small formation-energy difference of Yb under the experimental condition, mixed-site occupation cannot be excluded, which may explain the different occupation behaviors reported in previous studies. Thus, the DFT results provide thermodynamic insights into dopant incorporation while highlighting the critical role of synthesis conditions in determining the final cation distribution.

CONCLUSION

In summary, this work systematically demonstrates the distinct yet synergistic roles of ytterbium and magnesium dopants in stabilizing high-voltage $LiCoO_2$ cathodes. Through a comparative study, we confirm that the structural degradation and kinetic limitations of LCO at 4.6 V can be effectively addressed via a rational multi-element design. The large-radius Yb^{3+} ion primarily functions as a structural stabilizer by expanding the interlayer spacing and strengthening metal oxygen bonding, thereby suppressing phase transitions and oxygen release. Concurrently, the Mg^{2+} ion serves as a kinetic promoter, facilitating interfacial charge transfer and enhancing bulk lithium ion diffusion. This clear functional division, where Yb ensures structural integrity and Mg enables fast ion transport, forms the cornerstone of the observed electrochemical synergy. The superiority of this design is proven in the optimal Yb/Mg doping cathode (YM2-LCO), which achieves an exceptional balance between long-term cycling stability and high-rate capability, a combination unattainable by single element doping. Detailed kinetic analyses via EIS and GITT provide direct evidence of the lowest charge transfer resistance and highest lithium ion diffusion coefficient in the doping material. This work transcends conventional single element modification, offering a refined doping strategy based on functional complementarity. It provides both a fundamental understanding of dopant cooperation and a practical design principle for developing high-energy-density lithium-ion batteries.

REFERENCES

1. Zheng M., You Y. and Lu J. (2025). Understanding materials failure mechanisms for the optimization of lithium-ion battery recycling. *Nat. Rev. Mater.* **10**:355–368. DOI:10.1038/s41578-025-00783-5
2. Wu B., Chang Z., Chen Z., et al. (2025). Understanding degradation and enhancing cycling stability for high-voltage $LiCoO_2$-based Li-metal batteries. *Adv. Energy Mater.* **15**:2404028. DOI:10.1002/aenm.202404028
3. Fu A., Zhang Z., Lin J., et al. (2022). Highly stable operation of $LiCoO_2$ at cut-off >= 4.6 V enabled by synergistic structural and interfacial manipulation. *Energy Storage Mater.* **46**:406-416. DOI:10.1016/j.ensm.2022.01.033
4. Wang X., Wu Q., Li S., et al. (2021). Lithium-aluminum-phosphate coating enables stable 4.6 V cycling performance of $LiCoO_2$ at room temperature and beyond. *Energy Storage Mater.* **37**:67-76. DOI:10.1016/j.ensm.2021.01.031
5. Zhu Y., Wu D., Yang X., et al. (2023). Microscopic investigation of crack and strain of $LiCoO_2$ cathode cycled under high voltage. *Energy Storage Mater.* **60**:102828. DOI:10.1016/j.ensm.2023.102828
6. Konar R., Maiti S., Shpigel N., et al. (2023). Reviewing failure mechanisms and modification strategies in stabilizing high-voltage $LiCoO_2$ cathodes beyond 4.55 V. *Energy Storage Mater.* **63**:103001. DOI:10.1016/j.ensm.2023.103001
7. Zhang J., Wong D., Zhang Q., et al. (2023). Reducing Co/O band overlap through spin state modulation for stabilized high capability of 4.6 V $LiCoO_2$. *J. Am. Chem. Soc.* **145**:10208-10219. DOI:10.1021/jacs.3c01128
8. Harika V., Penki T., Fan T., et al. (2025). Stable LCO cathodes charged at 4.6 V for high energy secondary Li-ion batteries by one-pot dual metal fluorides coating. *Adv. Energy Mater.* **15**:2402794. DOI:10.1002/aenm.202402794
9. Li J., Lin C., Weng M., et al. (2021). Structural origin of the high-voltage instability of lithium cobalt oxide. *Nat. Nanotechnol.* **16**:599–605. DOI:10.1038/s41565-021-00855-x
10. Wang L., Chen B., Ma J., et al. (2018). Reviving lithium cobalt oxide-based lithium secondary batteries-toward a higher energy density. *Chem. Soc. Rev.* **47**:6505–6602. DOI:10.1039/c8cs00322j
11. Jiao S., Li Y., Lin T., et al. (2025). Achieving high-performance defect-free $LiCoO_2$ cathode via a dopant-free approach. *J. Am. Chem. Soc.* **147**:22839–22850. DOI:10.1021/jacs.5c05162
12. Zhang Z., Du P., Liu J., et al. (2025). Mechanisms of enhanced electrochemical performance by chemical short-range disorder in lithium oxide cathodes. *ACS Nano* **19**:6554–6562. DOI:10.1021/acsnano.4c17907
13. Zhang W., Zhang X., Cheng F., et al. (2023). Enabling stable 4.6 V $LiCoO_2$ cathode through oxygen charge regulation strategy. *J. Energy Chem.* **76**:557-565. DOI:10.1016/j.jechem.2022.09.034
14. Wang Q., Yao Z., Wang J., et al. (2024). Chemical short-range disorder in lithium oxide cathodes. *Nature* **629**:341–347. DOI:10.1038/s41586-024-07362-8
15. Sun C., Liao X., Xia F., et al. (2020). High-voltage cycling induced thermal vulnerability in $LiCoO_2$ cathode: Cation loss and oxygen release driven by oxygen vacancy

migration. *ACS Nano* **14**:6181–6190. DOI:10.1021/acsnano.0c02237
16. Wu Z., Zeng G., Yin J., et al. (2023). Unveiling the evolution of $LiCoO_2$ beyond 4.6 V. *ACS Energy Lett.* **8**:4806-4817. DOI:10.1021/acsenergylett.3c01954
17. Yu X. and Manthiram A. (2018). Electrode-electrolyte interfaces in lithium-based batteries. *Energy Environ. Sci.* **11**:527–543. DOI:10.1039/C7EE02555F
18. Lin C., Li J., Yin Z., et al. (2024). Structural understanding for high-voltage stabilization of lithium cobalt oxide. *Adv. Mater.* **36**:2307404. DOI:10.1002/adma.202307404
19. Chen J., Chen H., Zhang S., et al. (2022). Structure/interface coupling effect for high-voltage $LiCoO_2$ cathodes. *Adv. Mater.* **34**:2204845. DOI:10.1002/adma.202204845
20. Kong W., Zhou D., Zhang Q., et al. (2023). Adjusting the redox coupling effect via Li/Co anti-site defect for stable high-voltage $LiCoO_2$ cathode. *Adv. Funct. Mater.* **33**:2211033. DOI:10.1002/adfm.202211033
21. Park S., Seok J., Lee W. et al., (2025). Structural stabilization of 4.6 V $LiCoO_2$ through tri-site Co-doping with Al-Mg-F. *Small* **21**:2409892. DOI:10.1002/smll.202409892
22. Qu J., Wang B., Li J., et al. (2025). Separating Li-ion and electron conduction pathways to realize robust cathode interfaces. *J. Mater. Chem. A* **13**:28508–28520. DOI:10.1039/d5ta04002g
23. Luo D., Cui J., Zhang B., et al. (2021). Ti-based surface integrated layer and bulk doping for stable voltage and long life of Li-rich layered cathodes. *Adv. Funct. Mater.* **31**:2009310. DOI:10.1002/adfm.202009310
24. Hong Y., Huang X., Wei C., et al. (2020). Hierarchical defect engineering for $LiCoO_2$ through low-solubility trace element doping. *Chem* **6**:2759–2769. DOI:10.1016/j.chempr.2020.07.017
25. Liu T., Yan Z., Xin W., et al. (2025). Short-time and high-performance recovery of critical metal elements from spent ternary lithium-ion batteries by selective synergic coordination effect. *Adv. Funct. Mater.* **35**:2417883. DOI:10.1002/adfm.202417883
26. Zhou J., Liu Y., Peng Z., et al. (2024). Unveiling the tailorable electrochemical properties of zeolitic imidazolate framework-derived Ni-doped $LiCoO_2$ for lithium-ion batteries in half/full cells. *J. Energy Chem.* **93**:229–242. DOI:10.1016/j.jechem.2024.02.005
27. Wang Z., Li L., Sun Z., et al. (2024). Advances and perspectives in understanding the structure-redox relationship of layered Li-Co-Ni-Mn oxide cathode materials. *Prog. Mater. Sci.* **143**:101247. DOI:10.1016/j.pmatsci.2024.101247
28. Zhang Z., Wang J., Sun X., et al. (2024). Improved stability of single-crystal $LiCoO_2$ cathodes at 4.8 V through solvation structure regulation. *Adv. Funct. Mater.* **34**:2411409. DOI:10.1002/adfm.202411409
29. Huang Y., Zhu Y., Fu H., et al. (2021). Mg-pillared $LiCoO_2$: towards stable cycling at 4.6 V. *Angew. Chem. Int. Ed.* **60**:4682-4688. DOI:10.1002/anie.202014226
30. Wan J., Zhu J., Xiang Y., et al. (2021). Revealing the correlation between structure evolution and electrochemical performance of high-voltage lithium cobalt oxide. *J. Energy Chem.* **54**:786–794. DOI:10.1016/j.jechem.2020.06.027
31. Tang Y., Zhao J., Zhu H., et al. (2023). Towards extreme fast charging of 4.6 V $LiCoO_2$ via mitigating high-voltage kinetic hindrance. *J. Energy Chem.* **78**:13-20. DOI:10.1016/j.jechem.2022.11.044
32. Xia J., Zhang N., Yang Y., et al. (2023). Lanthanide contraction builds better high-voltage $LiCoO_2$ batteries. *Adv. Funct. Mater.* **33**:2212869. DOI:10.1002/adfm.202212869
33. Xia J., Zhang N., Yi D., et al. (2024). Stabilizing 4.6 V $LiCoO_2$ via Er and Mg trace doping at Li-site and Co-site respectively. *Small* **20**:2311578. DOI:10.1002/smll.202311578
34. Sun W., Yang J., Shi W., et al. (2024). A dual-Functional synergetic strategy enhances the interfacial and structural stability of $LiCoO_2$ at high voltage. *ACS Appl. Energy Mater.* **7**:6585–6597. DOI:10.1021/acsaem.4c01228
35. Ding X., Shi Y., Xu K., et al. (2025). A modification strategy for 4.6V $LiCoO_2$: Uniform nano-coating and multi-level structure via high-temperature calcination. *J. Power Sources* **660**:238477. DOI:10.1016/j.jpowsour.2025.238477.
36. Xia Y., Feng J., Li J., et al. (2024). Selective core-shell doping enabling high performance 4.6 V-LiCoO2. *J. Energy Chem.* **95**:684-693. DOI:10.1016/j.jechem.2024.04.004
37. Li X., Zhu X., Zhang Y., et al. (2025). Ternary inert element Co-doping: A new approach to stable 4.7 V $LiCoO_2$. *Adv. Mater.* **37**:2506228. DOI:10.1002/adma.202506228
38. Kresse G. and Furthmüller J. (1996). Efficient iterative schemes for ab initio total-energy calculations using a plane-wave basis set. *Phys. Rev. B* **54**:11169–11186. DOI:10.1103/PhysRevB.54.11169
39. Kresse G. and Furthmüller J. (1996). Efficiency of ab-initio total energy calculations for metals and semiconductors using a plane-wave basis set. *Comput. Mater. Sci.* **6**:15–50. DOI:10.1016/0927-0256(96)00008-0
40. Blöchl P. E. (1994). Projector augmented-wave method. *Phys. Rev. B* **50**:17953–17979. DOI:10.1103/PhysRevB.50.17953
41. Kresse G. and Joubert D. (1999). From ultrasoft pseudopotentials to the projector augmented-wave method. *Phys. Rev. B* **59**:1758–1775. DOI:10.1103/PhysRevB.59.1758
42. Perdew J. P., Burke K. and Ernzerhof M. (1996). Generalized gradient approximation made simple. *Phys. Rev. Lett.* **77**:3865–3868. DOI:10.1103/PhysRevLett.77.3865
43. Chase M. W. Jr. (1998). NIST-JANAF Thermochemical Tables. 4th ed. *J. Phys. Chem. Ref. Data Monograph* **9**:1-1951. DOI:10.1063/1.555974.
44. Reuter K. and Scheffler M. (2001). Composition, structure, and stability of RuO_2(110) as a function of oxygen pressure. *Phys. Rev. B* **65**:035406. DOI:10.1103/PhysRevB.65.035406
45. Shi W., Dong H., Yin J., et al. (2023). Synergetic effect of Ti-Mg-Sb tri-doping on enhanced electrochemical performance of $LiCoO_2$ at 4.6 V. *J. Alloys Compd.* **966**:171530. DOI:10.1016/j.jallcom.2023.171530
46. Xu S., Tan X., Ding W., et al. (2023). Promoting surface electric conductivity for high-rate $LiCoO_2$. *Angew. Chem. Int. Ed.* **62**:e202218595. DOI:10.1002/anie.202218595

FUNDING AND ACKNOWLEDGMENTS

We thank the financial support from the National Key Research and Development Program of China (2022YFA1207503) and the Natural Science Foundation of China (12427811). The funders had no role in study design, data collection and analysis, decision to publish, or preparation of the manuscript.

AUTHOR CONTRIBUTIONS

Jiaxing Wang and Peng Shi: writing—original draft, validation, methodology, investigation, formal analysis, data curation, conceptualization. Tao Zhou, Teng Wang and Zhangbin Cheng: methodology, investigation and analysis. Jingfeng Wang: resources and data curation. Guo Gao: writing—review and editing, supervision, resources, project administration, conceptualization. All authors contributed to the manuscript and approved the final version.

DECLARATION OF INTERESTS

The authors declare no competing interests.

DATA AND CODE AVAILABILITY

No new data were created or analyzed in this study.